



RESEARCH ARTICLE | FEBRUARY 15 2024

Including the parallel mass flow in calculating the steady-state solutions and stability of the momentum balance equations for a quasisymmetric stellarator

D. N. Michaelides; J. N. Talmadge  



Phys. Plasmas 31, 022504 (2024)

<https://doi.org/10.1063/5.0180082>



CrossMark

15 February 2024 16:03:53



AIP Advances

Why Publish With Us?



25 DAYS
average time
to 1st decision



740+ DOWNLOADS
average per article



INCLUSIVE
scope

[Learn More](#)

 AIP
Publishing

Including the parallel mass flow in calculating the steady-state solutions and stability of the momentum balance equations for a quasisymmetric stellarator

Cite as: Phys. Plasmas **31**, 022504 (2024); doi: 10.1063/5.0180082

Submitted: 6 October 2023 · Accepted: 11 January 2024 ·

Published Online: 15 February 2024



View Online



Export Citation



CrossMark

D. N. Michaelides and J. N. Talmadge^{a)}

AFFILIATIONS

HSX Plasma Laboratory, University of Wisconsin-Madison, Madison, Wisconsin 53706, USA

^{a)} Author to whom correspondence should be addressed: talmadge@wisc.edu

ABSTRACT

The Helically Symmetric Experiment (HSX) is a quasisymmetric stellarator with minimal parallel viscous damping in a helical direction. The parallel flow (V_{\parallel}) along the magnetic field is similarly weakly damped by viscosity. In this paper, the self-consistent steady-state parallel and poloidal momentum balance equations are used to show that a large V_{\parallel} on the order of the ion thermal velocity can increase the ion resonant radial electric field (E_r) beyond the value calculated using the typical approximation that V_{\parallel} is zero. By altering the damping of V_{\parallel} , either by degrading the quasisymmetry or varying the neutral density, the ion resonant E_r can shift in a controllable fashion. It is shown explicitly that there exist stable and unstable steady-state solutions in the two-dimensional space of V_{\parallel} and E_r . A stability analysis of each solution is performed by calculating the eigenvalues and eigenvectors of the Jacobian. The unstable solution corresponds to a saddle point in which the eigenvalues have opposite signs. The analysis leads to the conclusion that unstable solutions occur when the derivative of the total poloidal damping with respect to E_r is positive. A hysteresis in E_r and V_{\parallel} is observed when the radial current density is linearly increased to a maximum and then decreased back to zero. Jumps in the radial electric field and the parallel flow are observed as the radial current density drives the evolution from one stable point to the next. This result is similar to experimental data observed on several devices.

Published under an exclusive license by AIP Publishing. <https://doi.org/10.1063/5.0180082>

I. INTRODUCTION

The Helically Symmetric Experiment (HSX) belongs to a class of toroidal confinement devices known as quasisymmetric stellarators. All stellarators have the advantage as fusion reactors in possessing steady-state capability, low recirculating power, and the ability to avoid the disruptive termination of discharges. However, quasisymmetric stellarators have the additional advantage of having excellent confinement of fusion alpha particles and neoclassical transport comparable to that in an axisymmetric tokamak.^{1,2} They achieve this improvement in confinement over a conventional stellarator by preserving a continuous symmetry of the magnetic field strength $|B|$, rather than the vector \mathbf{B} as in a tokamak.

In conventional stellarators, $|B|$ varies in every direction on a flux surface leading to a large viscous damping of plasma flows. Because of the continuous symmetry in $|B|$, quasisymmetric stellarators have reduced parallel viscous damping of plasma flows in the direction of quasisymmetry. Reduced flow damping can aid in the sustainment of

large $\mathbf{E} \times \mathbf{B}$ velocity shear (where \mathbf{E} is the electric field) and in turn lead to the reduction of plasma turbulence and the generation of a transport barrier.³ In particular, the very high toroidal rotation in DIII-D is key to sustaining the very high confinement super H-mode in that device.⁴

Plasma flows and the radial electric field have been measured experimentally in HSX at relatively low rotation speeds. With a biased electrode at the plasma edge to spin the plasma, Gerhardt *et al.*⁵ observed with Mach probes that larger flows could be induced at slower spin-up times when the quasisymmetry was preserved than when it was degraded. Coronado and Talmadge⁶ considered the case when the viscous damping is linear with the flow and the plasma is in the plateau or Pfirsch-Schlüter collisionality regimes. With a constant bias on an electrode inserted into the plasma, the flow evolves as a sum of two exponentials with two distinct timescales that correspond to the weakest and the strongest momentum damping on a flux surface. As applied to HSX, the weakest damping is in the direction of

quasisymmetry, and the strongest damping is in a direction normal to that. Gerhardt *et al.*⁵ experimentally validated the two-timescale model.

In other experiments on HSX, Briesemeister *et al.*⁷ used charge exchange recombination spectroscopy (CHERS) to measure plasma flow up to 20 km/s that was oriented largely in the symmetry direction without any additional momentum input to the plasma. Kumar *et al.*⁸ showed that E_r as well as the mean ion parallel flow driven by viscosity could be determined by measuring the total ion parallel flow at two locations on a flux surface. Dobbins *et al.*⁹ observed that the ion parallel flow for the quasisymmetric configuration was smaller than predicted by the PENTA^{10,11} code. Because the viscous damping of the parallel flow for this configuration is small, an additional damping source due to collisions with neutrals was needed to bring the model into agreement with the measurements.

The previous experiments on HSX were all in the regime such that there was either no external momentum input to the plasma, or for the biased electrode case, E_r was much lower than the ion resonant electric field. In Shaing and Crume's¹² model of L–H transition, there is a bifurcation of the radial electric field due to the existence of a local maximum in the viscosity and a subsequent suppression of turbulence due to the shear in the $\mathbf{E} \times \mathbf{B}$ rotation. The peak in the viscosity occurs at the ion resonant E_r when the $\mathbf{E} \times \mathbf{B}$ drift cancels out the poloidal motion of a particle moving along the magnetic field. For a tokamak, this peak occurs when $M_p = -cE_r/B_p v_i \sim 1$, where c is the speed of light, B_p is the poloidal magnetic field strength, and v_i is the ion thermal speed. In this case, the viscosity maximum occurs when the net drift is along the toroidal direction so that ∇B and curvature drifts become unidirectional in the radial direction, as if there is no rotational transform at all. For a quasisymmetric stellarator like HSX, the maximum viscosity occurs when the net drift is along the helical direction of quasisymmetry. Shaing showed that in a conventional stellarator with multiple components of the magnetic field spectrum given by the toroidal mode number n and the poloidal mode number m , there would be multiple local peaks in the viscosity given by $M_p \sim |m - nq|/m$, where $q = 1/\iota$ is the safety factor and ι is the rotational transform.¹³ This expression, however, assumes that $V_{||} \sim 0$, which is reasonable for most stellarators because the plasma flow is strongly damped. As we show in this paper, it is not a good assumption for HSX.

For the most part, Shaing's viscosity model has been validated by experiments. Electrode biasing experiments on the TEXTOR tokamak showed that as the measured E_r in the plasma increased, the radial current density increased until it hit a maximum of around $M_p \sim 1$ (the magnetic field spectrum in a tokamak is dominated by the $m = 1$, $n = 0$ component) and then decreased.¹⁴ A similar result was observed on the CCT tokamak.¹⁵ For the IMS stellarator, the local peak in the radial current was observed in the range of $M_p \sim 10 - 15$ due to the helical components of the magnetic field spectrum and in agreement with the modeling.¹⁶ What has not been verified yet is the role of the parallel flow in determining the peak in the plasma viscosity.

In this paper, we apply Ref. 13 to HSX but do not assume that $V_{||} = 0$ as in that paper. We apply the steady-state parallel and poloidal momentum balance equations to solve self-consistently for E_r and $V_{||}$ as a function of the radial current drawn by a biased electrode in the plasma. This allows us to calculate how the damping of the parallel flow in different magnetic configurations of HSX affects the maximum

in the plasma viscosity. Also, we use numerically calculated Hamada basis vectors¹⁷ for HSX magnetic configurations instead of the large aspect ratio tokamak approximation¹⁸ that is assumed in the Shaing paper. In addition to the steady-state solutions, the stability of those solutions is analyzed to show that there are unstable solutions to the momentum balance equations. That unstable solutions exist was first pointed out in the original paper by Shaing and Crume¹² but little discussed since then. Also, that work only considered the variation of E_r , whereas we consider the two-dimensional problem in which the variables are E_r and $V_{||}$. One important outcome of the stability analysis is that it provides a possible model for the bifurcation and hysteresis observed in the TU-Heliac¹⁹ and LHD²⁰ due to the existence of an unstable branch of the momentum balance equations.

The remainder of this paper is organized as follows. In Sec. II, different magnetic configurations available in HSX and the plasma parameters that are used in the calculations are discussed. In Sec. III, it is shown using linear viscosity that in HSX, the parallel flow is dominated by the slow damping rate characteristic of the damping in the direction of quasisymmetry. The evolution of the radial electric field is dominated by the fast damping rate at the plasma core but dominated by the slow damping rate toward the edge. This is shown explicitly for the case when the plasma flow is small and the momentum balance equations can be solved analytically. This section provides the rationale for solving self-consistently for the parallel flow rather than setting it to zero when considering nonlinear viscosity. Section IV briefly reviews Shaing's model of nonlinear viscosity and a general expression for the resonant electric field that includes the parallel flow is obtained. In Sec. V, the steady-state solutions to the momentum balance equations are solved to show how $V_{||}$ affects the resonant electric field. It is shown explicitly how changing the damping of the parallel flow, either by changing the magnetic topology in HSX or controlling the neutral damping rate, can affect the resonant electric field. Section VI examines the stability of the steady-state solutions that were calculated in Sec. V. The eigenvalues of the Jacobian of the coupled differential equations indicate when the solutions are unstable, while the corresponding eigenvectors provide insight into how the time-dependent equations move toward or away from the fixed point. A physical explanation why certain solutions are unstable is obtained from the Jacobian. The existence of an unstable branch of the momentum balance equations can lead to the bifurcation and hysteresis observed experimentally in other devices. Finally, Sec. VII contains a summary and discussion of the results.

II. MAGNETIC GEOMETRIES AND PLASMA PARAMETERS

The HSX stellarator is a quasisymmetric stellarator with a four field-period coil set consisting of 48 non-planar modular coils. The magnetic field strength $|B|$ is approximately constant in a helical direction on a given flux surface, and the magnetic configuration has the property of quasihelical symmetry (QHS). The magnetic field spectrum on a flux surface is given by

$$\frac{B}{B_0} = \sum_{n,m} \epsilon_{n,m} \cos(n\zeta - m\theta), \quad (1)$$

where m and n are the poloidal and the toroidal mode numbers, θ and ζ are the poloidal and the toroidal angles, and $\epsilon_{n,m}$ is the mode amplitude for a given mode (n,m) . As explained in Sec. III, the calculations

presented here are in Hamada coordinates²¹ and the magnetic field spectrum is also calculated in this coordinate system. The dominant mode for the QHS configuration is (4,1), as seen in Fig. 1 (left). A unique property of the QHS configuration is that it has a high effective transform $t_{\text{eff}} = n - mt \approx 3$, where t is the nominal transform and varies from 1.05 at the magnetic axis to 1.12 at the edge. A high effective transform leads to small drifts of passing particles from a flux surface, small banana widths for trapped particles, low neoclassical transport, and small plasma currents.²²

Surrounding each of the main modular coils is a planar coil that can be energized in multiple configurations to change the magnetic field spectrum, raise or lower the rotational transform, and alter the magnetic well depth. With the auxiliary coils, it is possible to break the quasisymmetry and increase the parallel viscous damping in that direction. In addition to the QHS configuration, two additional configurations will be discussed in this paper. The Mirror has a (4,0) component in the spectrum in addition to the dominant (4,1) mode as seen in Fig. 1 (middle). A second configuration called F14 has a (4,0) mode that is smaller than that in Mirror as well as an (8,0) mode as seen in Fig. 1 (right). The parallel viscous damping, as well as the neoclassical transport, is higher in the Mirror configuration than in F14. However, the advantage of the F14 configuration experimentally is that on-axis ECRH heating and on-axis Thomson scattering measurements can be made, whereas the magnetic axis shifts in the Mirror configuration.²³

Plasmas in HSX are heated with up to two 28 GHz gyrotrons with a maximum power of 100 kW of electron cyclotron resonance heating (ECRH). The on-axis magnetic field is 1.0 T. Core electron temperatures up to 2.5 keV have been measured with Thomson scattering at a density of around $4.0 \times 10^{12} \text{ cm}^{-3}$.¹¹ However, the plasma parameters shown in Ref. 24 are used for the calculations reported in this paper. In this case, a methane plasma was used to improve the carbon signal so that the CHERS system could measure the C^{+6} ion temperature, as well as the parallel flow and the radial electric field. For these plasmas, the core electron temperature is around 1.5 keV and the

ion temperature is approximately 60 eV with a fairly flat profile. Consequently, the electrons are in the low-collisionality regime, while the ions are in the plateau regime.

There is a significant neutral density in HSX plasmas because of the relatively low electron density. For this reason, we include damping due to neutrals when solving the momentum balance equations. The DEGAS²⁵ code is used to calculate the atomic and the molecular neutral density in HSX. The output from the DEGAS code is scaled using measurements from an array of H_α detectors in HSX. The neutral density profile used in this paper is shown in Fig. 3 of Ref. 9. Damping due to atomic hydrogen is more important than molecular hydrogen, which has a much smaller cross section for momentum scattering. The atomic hydrogen density profile is about $1 \times 10^{10} \text{ cm}^{-3}$ in the core, rising to about $2 \times 10^{10} \text{ cm}^{-3}$ at the edge.

Damping due to neutrals dominates over parallel viscous damping in the direction of quasisymmetry and in the parallel flow, as shown in Sec. III. It has been observed experimentally in the paper by Gerhardt *et al.*⁵ that the measured slow damping rate in HSX is faster than the neoclassical model. In a manner similar to Ref. 5, we calculate the total damping using the measured profiles but also simulate possible non-neoclassical damping mechanisms by increasing the neutral density so that it becomes more like a proxy damping term. Also, in comparing the results of the momentum balance equations for different magnetic configurations, we assume that the plasma parameters are the same as for the QHS configuration so that any differences are due to the magnetic topology and not due to the parameters themselves.

III. USING LINEAR VISCOSITY TO DEMONSTRATE THE IMPORTANCE OF PARALLEL FLOW IN HSX

A common assumption for conventional stellarators is that the parallel flow is either zero or small because of the large viscous damping on a magnetic surface.^{10,13,26} We will show that the evolution of the parallel flow V_{\parallel} in HSX is only weakly damped and dominated by the slow damping rate in the direction of quasisymmetry throughout

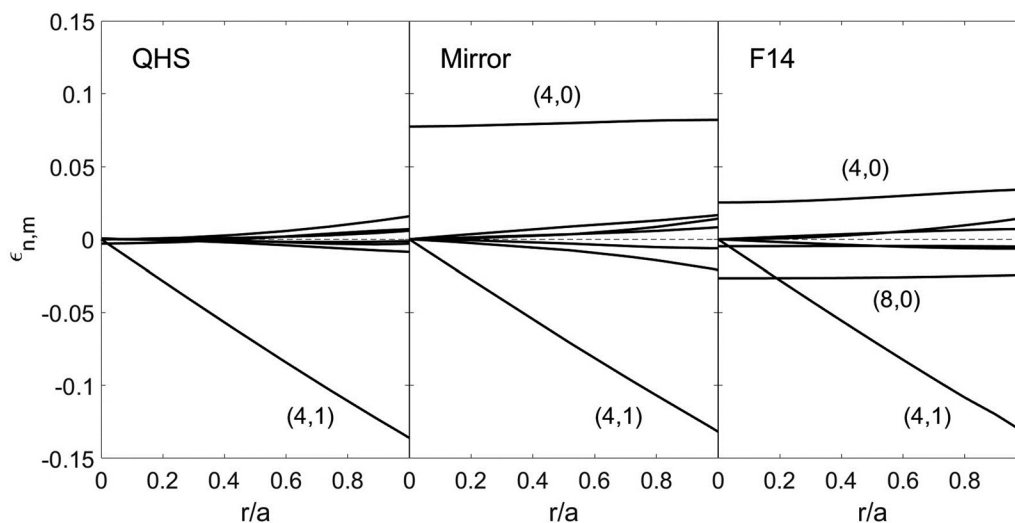


FIG. 1. The radial dependence of the seven leading terms of the magnetic field spectrum in Hamada coordinates for (left) the QHS configuration, (middle) the mirror configuration, and (right) the F14 configuration.

the plasma. For this reason, the parallel flow in HSX can be substantial and cannot be ignored. In contrast, the evolution of the radial electric field is a function of the radius in the plasma: strongly dominated by the fast damping rate in the core of the plasma and an increasing contribution of the slow damping rate toward the edge of the plasma.

In this section, we follow the methodology outlined in Ref. 6. Two features, in particular, allow us to solve the time-dependent momentum balance equations analytically to gain insight into the damping of plasma flows in HSX. The first is the use of Hamada coordinates in which the plasma flows and the magnetic field lines are straight. In this coordinate system, the contravariant components of the plasma flows and magnetic field, as well as the Jacobian, are constant on a flux surface. The second feature is the use of linear viscosity by which the viscosity is linearly proportional to the plasma flow. In the limit of small flows, the nonlinear viscosity model discussed in Sec. IV agrees with the linear viscosity model. However, when considering the evolution of plasma flows with the nonlinear viscosity, the equations have to be solved numerically. The information that we obtain in this section provides motivation for including the parallel flow in Shaing's model of nonlinear viscosity¹³ rather than setting it to zero.

The specific Hamada coordinates used in this paper differ slightly from that in Ref. 6 in that here we use the toroidal flux ψ as the radial coordinate, while the poloidal coordinate θ and the toroidal coordinate ζ vary between 0 and 2π , as in Ref. 17. Reference 6 used the volume enclosed by a flux surface V , as the radial coordinate while the two angle variables varied between 0 and 1. The result is that here the Jacobian is equal to $(1/4\pi^2)dV/d\psi$, while in Ref. 6 it is equal to 1.

The plasma consists of two species only, hydrogen ions and electrons, as well as a population of neutral hydrogen atoms. We neglect the heat flux and sum the momentum balance equations for the ions and electrons while ignoring the electron mass and the electron viscosity. The first order time-dependent momentum balance equations in the parallel and poloidal directions are

$$\begin{aligned} m_i N_i \frac{\partial \langle \mathbf{B} \cdot \mathbf{V}_i \rangle}{\partial t} &= -\langle \mathbf{B} \cdot \nabla \cdot \bar{\pi} \rangle - m_i N_i \nu_{in} \langle \mathbf{B} \cdot \mathbf{V}_i \rangle, \\ m_i N_i \frac{\partial \langle \mathbf{B}_P \cdot \mathbf{V}_i \rangle}{\partial t} &= -\langle \mathbf{B}_P \cdot \nabla \cdot \bar{\pi} \rangle - m_i N_i \nu_{in} \langle \mathbf{B}_P \cdot \mathbf{V}_i \rangle \\ &\quad - \frac{\sqrt{g} B^\zeta B^\theta}{c} \langle J_{\text{plasma}} \cdot \nabla \psi \rangle, \end{aligned} \quad (2)$$

where m_i is the ion mass, N_i is the ion density, $\langle \dots \rangle$ is the average over a magnetic surface, \mathbf{V}_i is the flow velocity, $\bar{\pi}$ is the viscosity tensor, ν_{in} is the ion-neutral collision frequency, $\mathbf{B}_P \equiv B^\theta \mathbf{e}_\theta$ (B^θ is the contravariant component of \mathbf{B} in the θ direction, \mathbf{e}_θ is the covariant basis vector), \sqrt{g} is the Jacobian, J_{plasma} is the radial current flowing in the plasma, and ψ is the toroidal flux. From the radial component of Ampère's law, we can relate the plasma current to the change in the radial electric field and an external current such as a biased electrode

$$\frac{\partial d\Phi}{\partial t} \langle \nabla \psi \cdot \nabla \psi \rangle = 4\pi [\langle J_{\text{plasma}} \cdot \nabla \psi \rangle + \langle J_{\text{external}} \cdot \nabla \psi \rangle], \quad (4)$$

where Φ is the plasma potential, $\frac{d\Phi}{d\psi}$ is a flux surface constant, and J_{external} is the external radial current density that, in this case, is the current density drawn by an electrode at time $t = t_0$ and held fixed.

In this section, we use the analytic linear viscosity model for ions in the plateau regime^{27,28} as shown explicitly in Ref. 5 under Eqs. (14a)

and (14b) in that paper. Inserting Eq. (4) into Eq. (3), and then combining with Eq. (2), there are two coupled ordinary differential equations for the variables λ and $\frac{d\Phi}{d\psi}$ in the matrix form

$$A \frac{dX}{dt} + BX = C, \quad (5)$$

where $X = \left[\frac{d\Phi}{d\psi}; \lambda \right]$ and λ is a flux surface constant such that $V_{\parallel} = \lambda B$ is the flux surface-averaged parallel flow driven by viscosity (as opposed to the Pfirsch-Schlüter component, which averages to zero over a flux surface). In this paper, all the calculations are done in cgs units and then converted to V_{\parallel} in km/s and E_r in kV/m with the following relationships: $V_{\parallel} \left(\frac{\text{km}}{\text{s}} \right) = \lambda \cdot B_0 (g) / 10^5$ and $E_r \left(\frac{\text{kV}}{\text{m}} \right) = -\frac{d\Phi}{d\psi} \cdot 2\sqrt{\pi} \psi B_0 \cdot 30$, where the toroidal flux $\psi \equiv \pi r^2 B_0$ and r is the minor radius.

For each magnetic configuration of HSX, the Hamada basis vectors are calculated numerically as outlined in Ref. 17 instead of assuming that the coordinate system is cylindrical or relying on a large aspect ratio tokamak approximation as described in Ref. 18. Written in Hamada coordinates and incorporating linear viscosity into the model, the coefficients A and B are matrices consisting of flux surface constants that do not depend on λ or $\frac{d\Phi}{d\psi}$ and so do not evolve in time. However, the term C in Eq. (5) depends on the time evolution of the external radial current density. We assume that $J_{\text{external}} = 0$ prior to time $t = t_0$ and is a constant at $t \geq t_0$.

The solution to Eq. (5), given in Eqs. (67a) and (67b) of Ref. 6, is the sum of two exponentials

$$\frac{d\Phi}{d\psi} = k_1 (1 - e^{\gamma_s(t-t_0)}) + k_2 (1 - e^{\gamma_f(t-t_0)}) + k_3, \quad (6)$$

$$\lambda = k_4 (1 - e^{\gamma_s(t-t_0)}) + k_5 (1 - e^{\gamma_f(t-t_0)}), \quad (7)$$

where γ_s, γ_f are the eigenvalues of Eq. (5) above and correspond to the slow and fast damping rates given by Eq. (60) in Ref. 6. The values of γ_s and γ_f are both negative. The terms k_1, k_2, k_4 , and k_5 are fixed in time and are dependent on $\langle J_{\text{external}} \cdot \nabla \psi \rangle$, the magnetic field spectrum, the Hamada basis vectors, the neutral density, and the plasma parameters. The constant k_3 is the initial steady-state value of $\frac{d\Phi}{d\psi} = -\frac{1}{en_i} \frac{dp}{d\psi}$, where p is the ion pressure, while the initial value for λ is zero.

From Eqs. (6) and (7), it can be determined how much the slow and fast timescales contribute to the parallel flow and the radial electric field. Figure 2 on the left shows the time evolution of E_r and V_{\parallel} after $t_0 = 1$ ms when a biased electrode at $r/a = 0.7$ draws current and the radial current density remains constant for 10 ms. This is for the QHS configuration. Also shown in the figure are the individual contributions of the slow and fast timescales to the evolution. The time evolution of E_r has a mixture of slow and fast timescales, while V_{\parallel} evolves almost entirely by the slow timescale characteristic of damping in the direction of quasisymmetry. Note that the fast decay rate has a very small contribution to the parallel flow and is negative, meaning that it subtracts from the contribution due to the slow timescale. On the right of the figure, the fractional contribution of the steady-state value of both the slow and fast timescales is plotted as a function of the normalized minor radius. The radial electric field is strongly dependent on the fast timescale in the core of the plasma, but the slow timescale dominates beyond the half-radius. In contrast, the parallel flow is strongly dependent on the slow decay rate throughout the plasma.

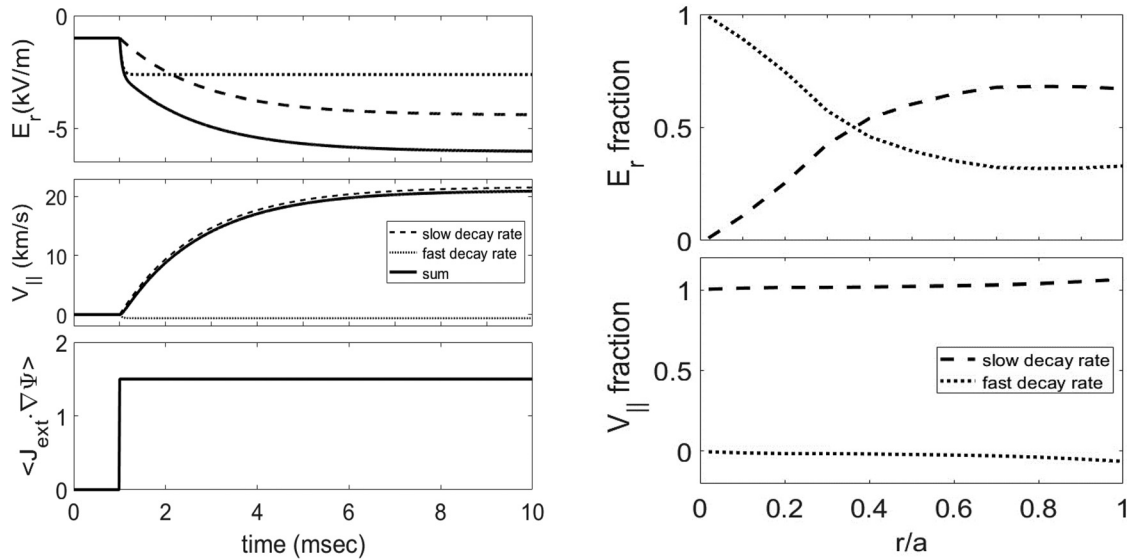


FIG. 2. (left) The radial current density (divided by 10^{10}) at $r/a = 0.7$ turns on at $t_0 = 1$ ms. Shown are the contributions of the slow (dashed) and fast (dotted) decay rates [see Eqs. (6) and (7)] to the evolution of E_r and $V_{||}$. (right) The steady-state fractional contributions of the slow and fast decay rates to E_r and $V_{||}$ as a function of the normalized minor radius.

Now that it is established that the parallel flow is almost completely dominated by the slow decay rate, it can be demonstrated that the magnitude of the steady-state value can be altered by varying the magnetic configuration in HSX or by changing the neutral density. Figure 3 shows the evolution of E_r and $V_{||}$ for the standard QHS configuration after a biased electrode is turned on and compared to two other configurations discussed in Sec. II, the F14 and the Mirror configurations. With the neutral damping held constant, the slow damping rate is increased for the F14 and Mirror configurations because of the degradation of the quasisymmetry. As a result, a lower steady-state $V_{||}$ is achieved in these configurations compared to the QHS configuration. It can also be seen that the fast damping rate that dominates the evolution of E_r early in time is similar for the three configurations, but because the slow damping rate dominates the evolution later in time, the steady-state electric field is also affected by the change in the parallel viscosity in the direction of quasisymmetry.

Figure 4 summarizes in a bar chart the relative values of the slow and fast damping rates for the three configurations, with and without neutral damping. For the experimental values of the neutral density in HSX, the QHS configuration has the smallest slow damping rate, followed by the F14 configuration and then the Mirror. The fast damping rates for QHS and Mirror are comparable and the F14 configuration slightly less. With neutral damping set to zero, the slow damping rate in the QHS configuration drops by a factor of 7, while the slow damping rate in the Mirror configuration changes by only 30%. For the fast damping rate, because the viscous damping is so high, the relative decrease in the damping rate is negligible when the neutral damping is set to zero.

From Eqs. (71) and (72) of Ref. 6, the total slow and fast damping rates are the sum of the ion neutral damping rate ν_{in} and the slow or the fast viscous damping rates. For the QHS configuration, $\nu_{in} = 487 \text{ s}^{-1}$, the slow viscous damping rate is only 78 s^{-1} so that the total slow damping rate is 565 s^{-1} . It is apparent that the total damping

in the direction of quasisymmetry is dominated by collisions with neutrals, given the current plasma parameters. Thus, the parallel flow is also strongly dominated by neutral damping. On the other hand, the evolution of the radial electric field is dominated by the fast damping

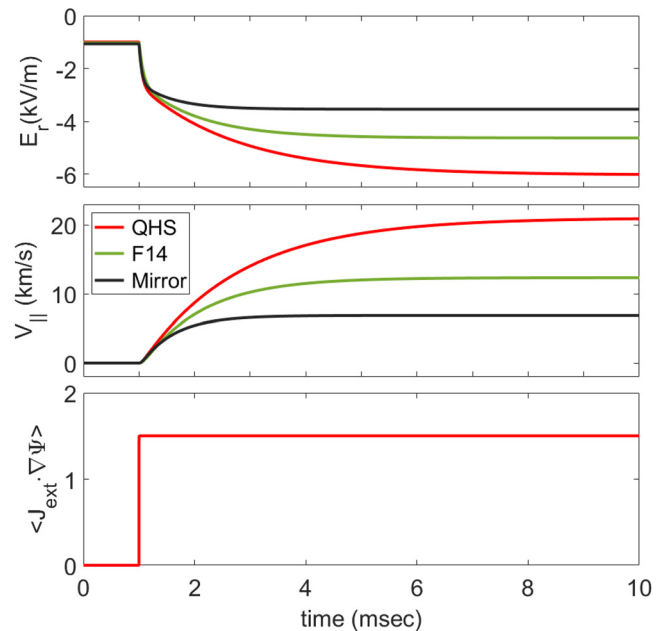


FIG. 3. The evolution of the radial electric field E_r and the parallel flow $V_{||}$ at $r/a = 0.7$ as a function of time after the external radial current density (divided by 10^{10}) turns on at $t_0 = 1$ ms for the magnetic configurations in HSX: the quasisymmetrically symmetric configuration (red), F14 configuration (green), and the Mirror configuration (black).

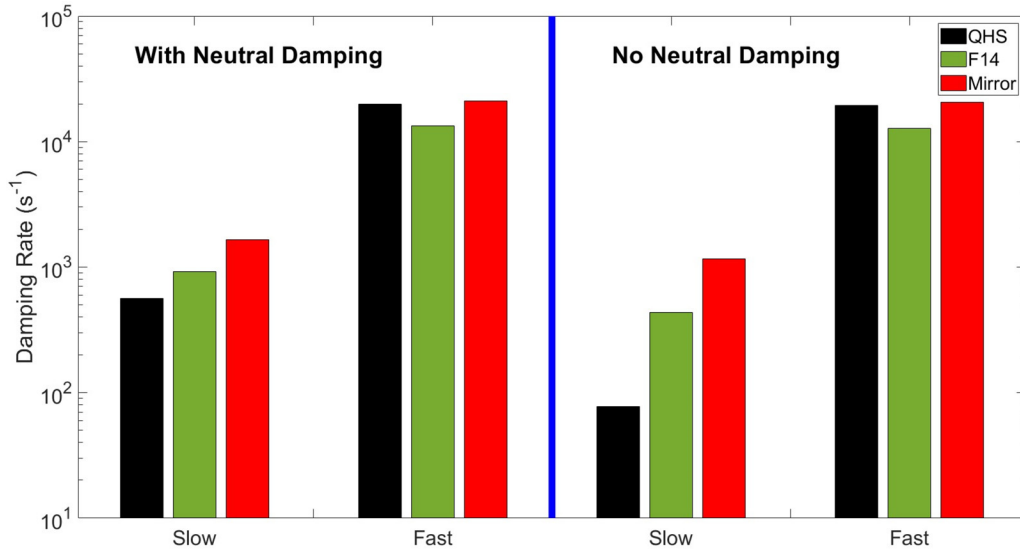


FIG. 4. Comparison of the slow $|\gamma_s|$ and fast $|\gamma_f|$ damping rates in the QHS, F14, and Mirror configurations of HSX, with (left) and without (right) neutral damping.

rate in the core of the plasma and thus relatively insensitive to the neutral density. However, further toward the edge, the evolution of E_r is increasingly dominated by the slow damping rate and hence is far more dependent on the neutral density. At this point, we have ignored anomalous sources of momentum damping such as that due to turbulence which could impact the damping in the direction of quasisymmetry. This will be discussed briefly in Sec. VII.

In Sec. IV, we will show that when nonlinear viscosity is considered, the parallel flow can have a strong impact on the ion resonant electric field. Moreover, in a subsequent section, it will be shown that it is possible to vary that impact by changing the parallel viscous damping as well as the neutral damping.

IV. NONLINEAR VISCOSITY AND THE IMPACT OF THE PARALLEL FLOW ON THE ION RESONANT ELECTRIC FIELD

Shaing extended his model of nonlinear viscosity as applied to tokamaks¹² to include the multiplicity of Fourier harmonics that constitute the magnetic field spectrum in conventional stellarators.¹³ This also extends the linear viscosity model discussed in Sec. III to include large flow velocities and the nonlinearity in the parallel viscosity. For conventional stellarators, it was shown that there could be a multiplicity of maxima in the viscosity, but for quasisymmetric stellarators, there is typically just one as in a tokamak. The model is valid in the plateau-Pfirsch-Schlüter regime so that the drift kinetic equation can be solved with a Krook collision operator. We will use the Hamada coordinate system given in Sec. III as well as in Ref. 17, rather than the coordinate system in Ref. 13.

The poloidal and toroidal viscosities are given as

$$\langle \mathbf{B}_t \cdot \nabla \cdot \boldsymbol{\pi} \rangle = \frac{\sqrt{\pi}}{4} v_{th} N_i m_i B \sum_{m,n} \left[I_{m,n} \epsilon_{m,n}^2 m (m V^\theta - n V^\zeta) + L_{m,n} \epsilon_{m,n}^2 m \frac{2}{5p} (m q^\theta - n q^\zeta) \right], \quad (8)$$

$$\langle \mathbf{B}_t \cdot \nabla \cdot \boldsymbol{\pi} \rangle = \frac{\sqrt{\pi}}{4} v_{th} N_i m_i B \sum_{m,n} \left[I_{m,n} \epsilon_{m,n}^2 (n q) (-m V^\theta + n V^\zeta) + L_{m,n} \epsilon_{m,n}^2 (n q) \frac{2}{5p} (-m q^\theta + n q^\zeta) \right], \quad (9)$$

where v_{th} is the ion thermal speed, $\epsilon_{m,n}$ is the amplitude of a component of the magnetic field spectrum as defined in Eq. (1), q is the safety factor, p is the ion pressure, and V^θ , V^ζ , q^θ , q^ζ are the contravariant components of the flow velocities and heat flux in the θ and ζ directions, respectively. In terms of the contravariant components of the magnetic field, the magnetic field vector is $\mathbf{B} = B^\theta \mathbf{e}_\theta + B^\zeta \mathbf{e}_\zeta \equiv \mathbf{B}_p + \mathbf{B}_t$. The integrals $I_{m,n}$ and $L_{m,n}$ are defined as

$$\left\{ \begin{array}{l} I_{m,n} \\ L_{m,n} \end{array} \right\} = \frac{1}{\pi} \int_0^\infty dx x^2 e^{-x} \left\{ \begin{array}{l} 1 \\ x - 5/2 \end{array} \right\} \int_{-1}^1 dy (1 - 3y^2)^2 \frac{v B^\theta}{B} R_{m,n}, \quad (10)$$

where $x = \frac{v^2}{v_{th}^2}$, $y = \frac{v_{||}}{v}$, v is the particle velocity and $v_{||}$ is the component of that velocity parallel to the magnetic field.

The nonlinearity in the viscosity and the local maxima are in the term $R_{m,n}$ which is defined as

$$R_{mn} = \left[\frac{\nu_K}{(m\omega_\theta - n\omega_\zeta)^2 + \nu_K^2} \right], \quad (11)$$

where ν_K is the Krook collision frequency and the terms ω_θ and ω_ζ are defined as

$$\omega_\theta = \left(\frac{v_{||} + V_{||}}{B} \right) B^\theta + V_E^\theta, \quad (12)$$

$$\omega_\zeta = \left(\frac{v_{||} + V_{||}}{B} \right) B^\zeta + V_E^\zeta. \quad (13)$$

Here, $V_{||}$ is the parallel mass flow velocity and V_E^θ and V_E^ζ are the contravariant components of the $\mathbf{E} \times \mathbf{B}$ drift velocity. From Eqs. (23a)

and (23b) from Ref. 6 and keeping the term for the Jacobian (that is, not setting it to 1 as was done in that paper), the contravariant components of the velocity are

$$V^\theta = \frac{c}{\sqrt{g}B^z} \left(\frac{d\Phi}{d\psi} + \frac{1}{eN_i} \frac{dp}{d\psi} \right) + \lambda B^\theta, \quad (14)$$

$$V^z = \lambda B^z, \quad (15)$$

so that $V_E^\theta = \frac{c}{(\sqrt{g}B^z)} \frac{d\Phi}{d\psi}$ and $V_E^z = 0$.

From the resonant term in the denominator of R_{mn} , an approximate expression for the ion resonant electric field can be obtained when $m\omega_\theta - n\omega_z = 0$ and using Eqs. (12)–(15), so that for a given component (n,m) of the magnetic field spectrum

$$m \left(\frac{v_\parallel + V_\parallel}{B} \right) B^\theta + \frac{mc}{\sqrt{g}B^z} \frac{d\Phi}{d\psi} - n \left(\frac{v_\parallel + V_\parallel}{B} \right) B^z = 0. \quad (16)$$

Given that in the straight-line coordinate system $B^\theta = \tau = \frac{1}{q}$ then

$$c \frac{d\Phi}{d\psi} = - \frac{m - nq}{m} \frac{q(B^\theta)^2}{B} (v_\parallel + V_\parallel) \sqrt{g}. \quad (17)$$

In Sec. V, the numerical evaluation of B^θ and \sqrt{g} in Eq. (17) will be used as outlined in Ref. 17. However, to about a 20% accuracy, a large aspect ratio tokamak approximation, also given in Ref. 17 for the coordinate system used here, is useful. Given that $B^\theta \cong \frac{B_0}{R}$, $\sqrt{g} = \frac{dV}{d\psi} / (4\pi^2)$, $\frac{dV}{d\psi} \cong \frac{2\pi R}{B_0} \frac{d\Phi}{dr} = \frac{d\Phi}{d\psi} 2B_0 \pi r$, and $\tau = \frac{RB_0}{rB_0}$ (this B_p , which is not a vector, is the poloidal component of the magnetic field in cylindrical coordinates), and R is the major radius of the device, then with $E_r = -\frac{d\Phi}{dr}$

$$cE_{res} \cong \frac{m - nq}{m} (v_\parallel + V_\parallel) B_p, \quad (18)$$

where E_{res} is the ion resonant radial electric field. Using the typical assumption for conventional stellarators that $V_\parallel \sim 0$ and for $v_\parallel \sim v_{th}$, the expression given by Shaing is recovered that

$$M_p \equiv - \frac{cE_{res}}{B_p v_{th}} \cong - \frac{m - nq}{m}, \quad (19)$$

where M_p is the poloidal Mach number. For a tokamak with $m = 1$, $n = 0$, the viscosity peaks at a poloidal Mach number of 1, while for HSX with $m = 1$, $n = 4$ and $q \sim 1$, the viscosity peaks at a poloidal Mach number of about 3.

It can be observed from Eqs. (17) or (18) that if V_\parallel is on the order of or greater than the ion thermal velocity, then the ion resonant electric field E_{res} will shift appreciably. Typical ion thermal velocities in HSX are on the order of 60–100 km/s. It has been observed experimentally in HSX that the parallel flow without any momentum input into the plasma can be as high as 20 km/s toward the plasma core and decreasing toward the edge.²⁹ Figure 5 shows a plot of the poloidal viscosity, given in Eq. (8), for the QHS configuration of HSX at $r/a = 0.7$ as a function of the radial electric field for the case when $V_\parallel = 0$ as well as for $V_\parallel = 20$ km/s. It is assumed here, as in Sec. III, that the heat flux is zero because of the relatively flat ion temperature profile measured in HSX. For zero parallel flow, E_{res} occurs at 17.9 and -18.0 kV/m, while for $V_\parallel = 20$ km/s, $E_{res} = 14.7$ and -21.2 kV/m, a

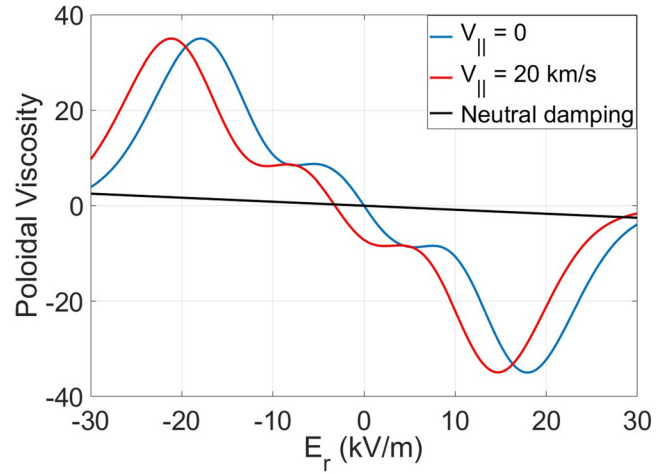


FIG. 5. Poloidal viscosity as a function of E_r for $V_\parallel = 0$ (blue) and $V_\parallel = 20$ km/s (red). Also shown is the contribution of neutral damping (black) to the total poloidal damping.

change of less than 20%. However, with additional momentum input into the plasma, such as with a biased electrode, it could be possible to have a much larger shift in the ion resonant electric field. This will be discussed in Sec. V. Also shown in the figure, for comparison, is the neutral contribution to the total poloidal damping. Consistent with the linear viscosity model, neutral damping has a minimal contribution to poloidal damping at low E_r . However, at an electric field higher than E_{res} , the poloidal viscosity drops, and neutral damping can be significant.

V. USING THE STEADY-STATE SOLUTIONS TO THE MOMENTUM BALANCE EQUATIONS TO FIND THE RESONANT ELECTRIC FIELD

As discussed in Sec. III, the parallel flow is weakly damped in HSX, compared to other stellarators, because HSX possesses a quasi-helically symmetric field. In Sec. IV, it was shown that if the parallel flow is on the order of or greater than the ion thermal velocity, then the ion resonant electric field can be shifted. In this section, the coupled steady-state momentum balance equations are solved self-consistently for the parallel flow and the radial electric field when driven by an external momentum source such as a biased electrode. Changing the damping due to neutrals or altering the parallel viscosity can control the parallel flow and thereby the resonant electric field. In this section, we also show the existence of multiple solutions to the momentum balance equations. In Sec. VI, we will demonstrate that not all of the equilibrium solutions are stable.

The steady-state equations to be solved for $\frac{d\Phi}{d\psi}$ and λ are obtained from Eqs. (2)–(4) from Sec. III. If at time $t = t_0$ a biased electrode is turned on so that $\langle \mathbf{J}_{external} \cdot \nabla \psi \rangle$ is a constant, initially $\langle \mathbf{J}_{plasma} \cdot \nabla \psi \rangle$ will start out as zero and over the characteristic damping times of the plasma will increase so that in steady-state $\langle \mathbf{J}_{plasma} \cdot \nabla \psi \rangle = -\langle \mathbf{J}_{external} \cdot \nabla \psi \rangle$. That is, a return current inside the plasma builds up until it equals the external current and through Eq. (4), the radial electric field stops changing. The two steady-state equations to be solved are

$$\langle \mathbf{B} \cdot \nabla \cdot \bar{\pi} \rangle + m_i N_i v_{in} \langle \mathbf{B} \cdot \mathbf{V}_i \rangle = 0, \quad (20)$$

$$\langle \mathbf{B}_p \cdot \nabla \cdot \tilde{\pi} \rangle + m_i N_i \nu_{in} \langle \mathbf{B}_p \cdot \mathbf{V}_i \rangle = \frac{\sqrt{g} B^{\zeta} B^{\theta}}{c} \langle \mathbf{J}_{external} \cdot \nabla \psi \rangle, \quad (21)$$

where the viscosity terms are given in Eqs. (8) and (9) and noting that $\mathbf{B} = \mathbf{B}_p + \mathbf{B}_t$.

A vector \mathbf{A} can be written in terms of the covariant and contravariant basis vectors, respectively, as $\mathbf{A} = A^{\psi} \mathbf{e}_{\psi} + A^{\theta} \mathbf{e}_{\theta} + A^{\zeta} \mathbf{e}_{\zeta} = A_{\psi} \nabla \psi + A_{\theta} \nabla \theta + A_{\zeta} \nabla \zeta$, where $B^{\psi} \equiv \mathbf{B} \cdot \nabla \psi = V^{\psi} = 0$ and $\mathbf{e}_i \cdot \nabla \psi = \delta_j^i$. Thus, $\langle \mathbf{B} \cdot \mathbf{V} \rangle = \langle B_{\theta} \rangle V^{\theta} + \langle B_{\zeta} \rangle V^{\zeta}$ and V^{θ} and V^{ζ} can be taken outside of the flux-surface average denoted by the brackets since they are already constants on a surface in Hamada coordinates. However, from Ref. 17, $\langle B_{\theta} \rangle$ is proportional to the toroidal current within a flux surface, and for this paper, the plasma is assumed to be current-free. The term $\langle B_{\zeta} \rangle$ can then be written in terms of the contravariant components of the magnetic field $\langle B_{\zeta} \rangle = \langle \mathbf{B} \cdot \mathbf{e}_{\zeta} \rangle = B^{\theta} \langle \mathbf{e}_{\theta} \cdot \mathbf{e}_{\zeta} \rangle + B^{\zeta} \langle \mathbf{e}_{\zeta} \cdot \mathbf{e}_{\zeta} \rangle$. In a similar manner, $\langle \mathbf{B}_p \cdot \mathbf{V} \rangle = B^{\theta} \langle V_{\theta} \rangle = B^{\theta} V^{\theta} \langle \mathbf{e}_{\theta} \cdot \mathbf{e}_{\theta} \rangle + B^{\zeta} V^{\zeta} \langle \mathbf{e}_{\theta} \cdot \mathbf{e}_{\zeta} \rangle$. The two expressions for neutral damping in Eqs. (20) and (21) are therefore

$$m_i N_i \nu_{in} \langle \mathbf{B} \cdot \mathbf{V}_i \rangle = m_i N_i \nu_{in} \left(B^{\theta} V^{\zeta} \langle \mathbf{e}_{\theta} \cdot \mathbf{e}_{\zeta} \rangle + B^{\zeta} V^{\zeta} \langle \mathbf{e}_{\zeta} \cdot \mathbf{e}_{\zeta} \rangle \right), \quad (22a)$$

$$m_i N_i \nu_{in} \langle \mathbf{B}_p \cdot \mathbf{V}_i \rangle = m_i N_i \nu_{in} \left(B^{\theta} V^{\theta} \langle \mathbf{e}_{\theta} \cdot \mathbf{e}_{\theta} \rangle + B^{\zeta} V^{\zeta} \langle \mathbf{e}_{\theta} \cdot \mathbf{e}_{\zeta} \rangle \right), \quad (22b)$$

where the contravariant components of the flow velocity are from Eqs. (14) and (15).

The viscosity and neutral damping terms, shown in Fig. 5 and corresponding to the individual terms on the left side of Eq. (21), are summed and plotted in Fig. 6. In steady-state, this is equal to the right-hand side of Eq. (21), $\frac{\sqrt{g} B^{\zeta} B^{\theta}}{c} \langle \mathbf{J}_{external} \cdot \nabla \psi \rangle$. For a fixed value of the external current density, illustrated by the horizontal lines in the figure, multiple solutions to Eq. (21) may exist. Both Eqs. (20) and (21) are needed to solve for a particular solution in terms of $\frac{d\Phi}{d\psi}$ and λ , but in general, there are three categories of solutions. The solution that

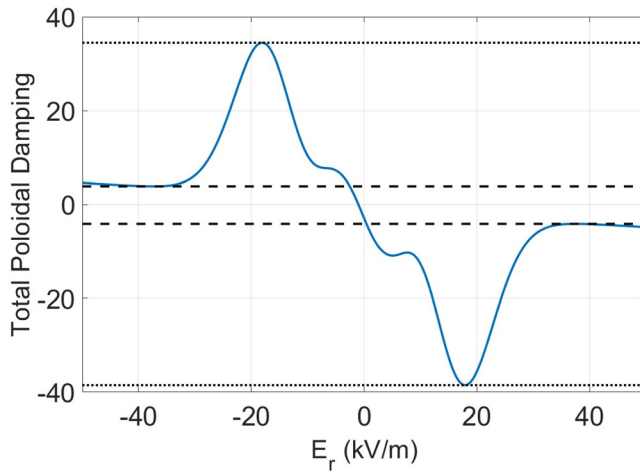


FIG. 6. The sum of the poloidal viscous and neutral damping as a function of the radial electric field with $V_{||} = 0$. In between the dashed lines, there is only one solution to Eq. (21). Between the dashed and dotted lines, there are two solutions. At the resonant electric field, which corresponds to the maximum in viscosity, there is only one solution. A third solution can also exist and is discussed in the following section.

corresponds to an increase in the viscosity is defined as solution 1. The solution that occurs in the region of decreasing viscosity is solution 2. Finally, there may be another solution that occurs far past the peak in viscosity when the total damping is once again increasing with respect to the radial electric field. This is the case with neutral damping or possibly other mechanisms in which the damping increases with the electric field. This is defined as solution 3. For the purpose of this section, we are interested in finding the resonant electric field, which coincides with the viscosity maximum. This is the intersection of solutions 1 and 2. In Sec. VI, we will consider solution 3 in more detail.

From Eqs. (20) and (21), E_r and $V_{||}$ are calculated as a function of the external surface averaged radial current density $\langle \mathbf{J}_{external} \cdot \nabla \psi \rangle$. This is plotted in Fig. 7 for the parallel viscosity appropriate to the QHS configuration and with neutral damping consistent with the experimental measurements. As the external current density increases, the parallel flow increases as does the radial electric field until the point where there is only one solution, which corresponds to the resonant electric field at the viscosity maximum. At this point, $V_{||}$ is -167 km/s for a negative current density and 150 km/s when the current density is positive. For these values of the parallel flow, the resonant electric field corresponds to $E_{res} = 44.8$ and -42.1 kV/m. This is over a factor of 2 greater than the value with zero parallel flow, which is about ± 18 kV/m from Fig. 5. The validity of very high parallel flows in this case is discussed more in Sec. VII.

From Eq. (17), it can be seen that the resonant electric field depends on the parallel flow, and from Fig. 3, it can be observed that increasing the damping of the parallel flow with viscosity can decrease the steady-state parallel flow. Therefore, one would expect that in the Mirror configuration, in which the quasihelical symmetry is degraded, the resonant electric field might be lower than it is for the QHS configuration of Fig. 7. Figure 8 shows E_r and $V_{||}$ as a function of the external radial current density using the same scale as Fig. 7 for comparison. At the viscosity maxima, $V_{||} = -75.6$ and 71.2 km/s and $E_{res} = 25.9$ and

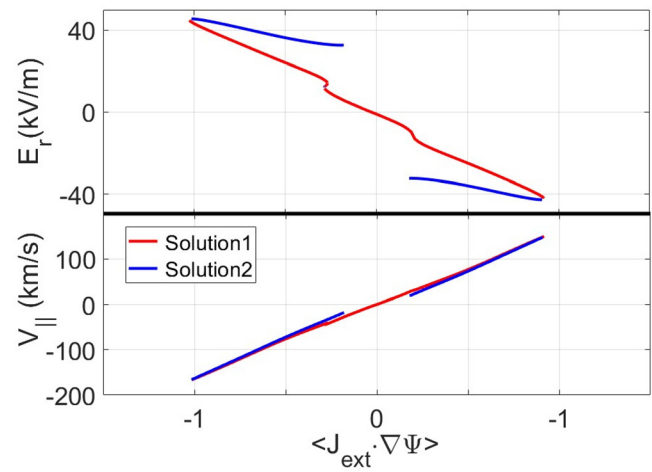


FIG. 7. E_r (top) and $V_{||}$ (bottom) as a function of the radial current density $\langle \mathbf{J}_{external} \cdot \nabla \psi \rangle$ (divided by 10^{11}) for the QHS configuration and with the experimental neutral density. Shown are solutions 1 (red), which are in the region before the peak in viscosity, and solutions 2 (blue), which are in the region where the viscosity is decreasing. The resonant electric fields are determined from the intersection of the 2 solutions and correspond to the extrema of the radial current density.

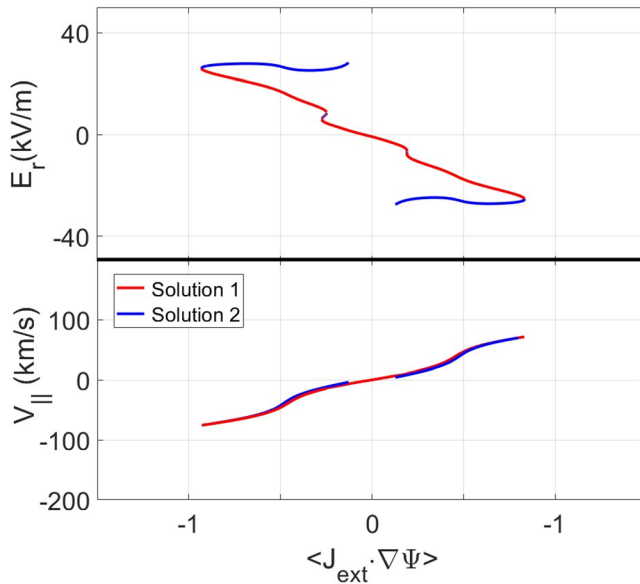


FIG. 8. E_r (top) and $V_{||}$ (bottom) as a function of the radial current density $\langle J_{\text{external}} \cdot \nabla \psi \rangle$ (divided by 10^{11}) for the Mirror configuration and with the experimental neutral density. Shown are solutions 1 (red), which are in the region before the peak in viscosity, and solutions 2 (blue), which are in the region where the viscosity is decreasing.

−25.5 kV/m, respectively. Note that for the Mirror configuration, the steady-state parallel flow at the resonant electric field is about half that in the QHS configuration and the resonant electric field drops by about 40%. As discussed in Sec. II, Mirror has an $n = 4$, $m = 0$ term in the magnetic field spectrum in addition to the main $n = 4$, $m = 1$ quasi-helical term. However, this additional term does not lead to an additional peak in the poloidal viscosity because of the $m = 0$ symmetry. Hence, the single peak observed in the Mirror configuration is still due to the $n = 4$, $m = 1$ term. If one were to ignore the parallel flow, then it would be expected that the QHS and Mirror configurations would have the same resonant electric field as given in Eq. (19). These results indicate that the two configurations would have very different resonant electric fields because the damping of the parallel flow is different for the two configurations.

From the discussion regarding Fig. 4, the damping of the parallel flow in the QHS configuration is dominated by damping due to neutrals since the viscous damping is so small. Hence, another method of increasing the damping of the parallel flow is to increase the neutral density. Figure 9 shows E_r and $V_{||}$ as a function of the external radial current density for the QHS configuration but with ten times the neutral density that is observed experimentally. At the viscosity maxima, $V_{||} = -16.5$ and 14.7 km/s, while $E_{\text{res}} = 21.1$ and -21.5 , respectively. Because of the very large neutral damping, the steady-state parallel flow is down by a factor of about 10 compared to Fig. 7 and the resultant resonant electric field is getting close to the $V_{||} = 0$ value of ± 18 kV/m.

Figure 10 shows a plot of the resonant electric field E_{res} as a function of the parallel flow $V_{||}$ for multiple magnetic configurations and different neutral densities. Shown at $V_{||} = 0$ is the reference case for HSX when the parallel flow is ignored; $E_{\text{res}} = \pm 18$ kV/m. For the

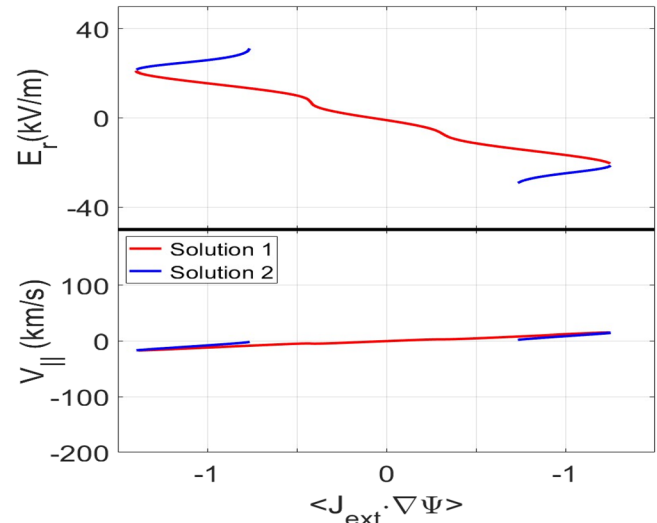


FIG. 9. E_r (top) and $V_{||}$ (bottom) as a function of the radial current density $\langle J_{\text{external}} \cdot \nabla \psi \rangle$ (divided by 10^{11}) for the QHS configuration but with 10 times the experimental neutral density. Shown are solutions 1 (red), which are in the region before the peak in viscosity, and solutions 2 (blue), which are in the region where the viscosity is decreasing.

experimental neutral density, the steady-state parallel flow is large and E_{res} increases. For the same neutral density, changing the magnetic configuration to the Mirror lowers the parallel flow and the resonant electric field. As expected from Fig. 3, the F14 configuration has a steady-state parallel flow and E_{res} intermediate to the QHS and Mirror configurations. Increasing the neutral density by a factor of 10 in the QHS configuration brings the resonant electric field almost back to the

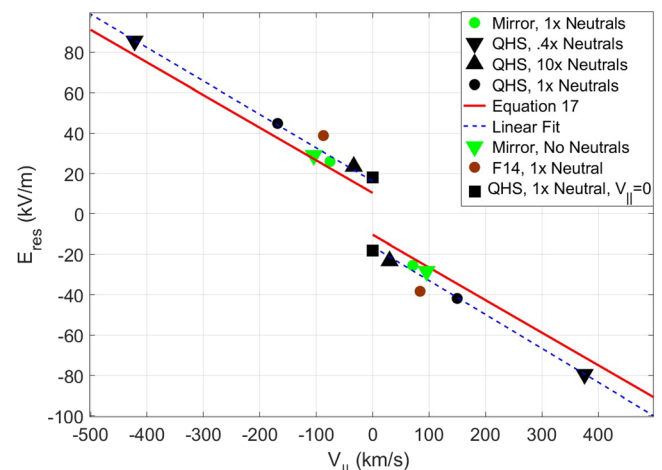


FIG. 10. The resonant electric field as a function of the parallel velocity at the resonance for different magnetic configurations and neutral densities. The QHS configuration is shown in black, Mirror in green, and F14 configuration in brown. Circles represent the experimental neutral density, other shapes represent different neutral densities. Also plotted are a linear regression of the HSX cases (blue dotted line) and the analytical solution for the resonant electric field as a function of the parallel flow, Eq. (17) (red).

$V_{||} = 0$ case. The analytic expression given in Eq. (17) is shown to be a good fit to the numerical data.

VI. THE STABILITY OF EQUILIBRIUM SOLUTIONS AND HYSTERESIS IN THE PLASMA FLOW

In Sec. V, it was observed that there could be at least two steady-state solutions to the momentum balance equations. For neutral densities that correspond to the experimental value, there is a third solution that exists at electric fields far beyond the peak in the poloidal viscosity. In this section, we consider the case that the third solution is close to the other two solutions and analyze the stability of all three solutions as well as transitions between the solutions. The focus in this section is when the neutral density is ten times the experimental values as discussed with regard to Fig. 9. The motivation for this particular value of the neutral density is that it corresponds roughly to an “*ad hoc*” adjustment of the slow damping rate in earlier experiments to bring the experimental data in line with the model discussed in Sec. III.⁵ This is discussed further in Sec. VII.

Figure 11 shows E_r and $V_{||}$ as a function of the radial current density, $\langle J_{\text{external}} \cdot \nabla \psi \rangle$, with the two solution spaces denoted by the colors red and blue as before, depending on whether the electric field is lower or higher than the resonant electric field. A third solution space, shown in green, is in the region where the total poloidal damping is again increasing with E_r . For this section, we are focusing only on the positive current density. One interesting aspect of the figure is that in the third solution space, the radial electric field is steadily increasing, while the parallel flow is decreasing to zero. Drawing on the physical model discussed in Shaing and Callen,³⁰ the radial electric field drives an $E \times B$ flow that is perpendicular to the field line. Parallel viscosity then drives a parallel flow so that the net flow is in the direction of minimal gradient in $|B|$. For HSX, this is in the direction of quasihelical

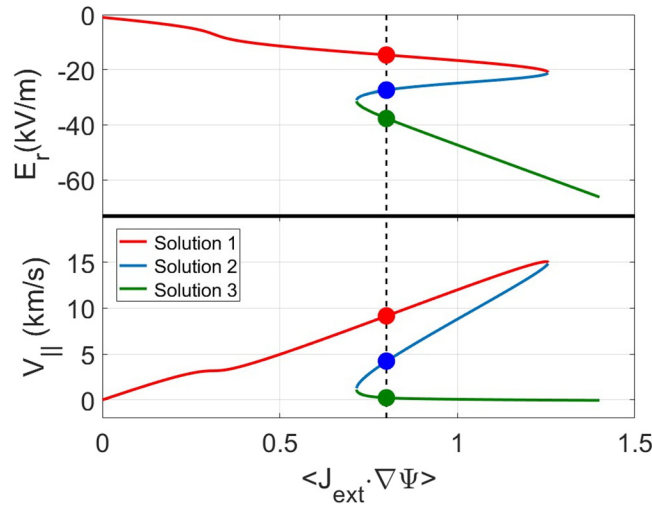


FIG. 11. E_r (top) and $V_{||}$ (bottom) as a function of the radial current density $\langle J_{\text{external}} \cdot \nabla \psi \rangle$ (divided by 10^{11}) for the QHS configuration but with 10 times the experimental neutral density. Shown are solutions 1 (red) in the region before the peak in viscosity, solutions 2 (blue) in the region where the viscosity is decreasing, and solutions 3 (green) in the region where the poloidal damping is once again increasing due to neutral damping.

symmetry. As the parallel viscosity becomes negligible at high values of E_r , the parallel flow also becomes negligible.

Also shown in Fig. 11 are three specific steady-state solutions to the coupled momentum balance equations that correspond to a value of $\langle J_{\text{external}} \cdot \nabla \psi \rangle = 8.0 \times 10^{10}$. The three solutions corresponding respectively to the red, blue, and green regions are $E_r = -14.7$ kV/m, $V_{||} = 9.2$ km/s, $E_r = -27.4$ kV/m, $V_{||} = 4.2$ km/s, and $E_r = -37.7$ kV/m, $V_{||} = 0.2$ km/s. The same color coding will be used later in this section when analyzing the stability of these solutions.

To analyze the stability of the three solutions, the expression for $\langle J_{\text{plasma}} \cdot \nabla \psi \rangle$ in Eq. (4) is substituted into Eq. (3) while keeping the time derivatives on the left-hand side of the equation

$$m_i N_i \frac{\partial \langle \mathbf{B}_p \cdot \mathbf{V}_i \rangle}{\partial t} + \frac{\sqrt{g} B^{\zeta} B^{\theta}}{4\pi c} \frac{\partial \Phi'}{\partial t} \langle \nabla \psi \cdot \nabla \psi \rangle = -\langle \mathbf{B}_p \cdot \nabla \cdot \bar{\pi} \rangle - m_i N_i \nu_{in} \langle \mathbf{B}_p \cdot \mathbf{V}_i \rangle + \frac{\sqrt{g} B^{\zeta} B^{\theta}}{c} J_{\text{external}} \cdot \nabla \psi, \quad (23)$$

where $\Phi' \equiv \frac{d\Phi}{dt}$. Since $\mathbf{B}_p \equiv B^{\theta} \mathbf{e}_{\theta}$,

$$\frac{\partial \langle \mathbf{B}_p \cdot \mathbf{V}_i \rangle}{\partial t} = B^{\theta} \langle \mathbf{e}_{\theta} \cdot \mathbf{e}_{\theta} \rangle \frac{\partial V^{\theta}}{\partial t} + B^{\theta} \langle \mathbf{e}_{\theta} \cdot \mathbf{e}_{\zeta} \rangle \frac{\partial V^{\zeta}}{\partial t} \quad (24)$$

and from Eqs. (14) and (15),

$$\frac{\partial \langle \mathbf{B}_p \cdot \mathbf{V}_i \rangle}{\partial t} = B^{\theta} \langle \mathbf{e}_{\theta} \cdot \mathbf{e}_{\theta} \rangle \frac{c}{\sqrt{g} B^{\zeta}} \frac{\partial \Phi'}{\partial t} + \frac{\partial \lambda}{\partial t} \left[B^{\theta} B^{\theta} \langle \mathbf{e}_{\theta} \cdot \mathbf{e}_{\theta} \rangle + B^{\theta} B^{\zeta} \langle \mathbf{e}_{\theta} \cdot \mathbf{e}_{\zeta} \rangle \right]. \quad (25)$$

However, for the term in the square brackets on the right,

$$\langle \mathbf{e}_{\theta} \cdot \mathbf{e}_{\theta} \rangle B^{\theta} + \langle \mathbf{e}_{\theta} \cdot \mathbf{e}_{\zeta} \rangle B^{\zeta} = \langle B_{\theta} \rangle. \quad (26)$$

As before, $\langle B_{\theta} \rangle$ for a currentless stellarator is zero, so the term multiplying $\frac{\partial \lambda}{\partial t}$ vanishes and Eq. (23) can then be written as

$$\left[\frac{m_i N_i c \langle B_p^2 \rangle}{\sqrt{g} B^{\theta} B^{\zeta}} + \frac{\sqrt{g} B^{\zeta} B^{\theta}}{4\pi c} \langle \nabla \psi \cdot \nabla \psi \rangle \right] \frac{\partial \Phi'}{\partial t} = -\langle \mathbf{B}_p \cdot \nabla \cdot \bar{\pi} \rangle - m_i N_i \nu_{in} \langle \mathbf{B}_p \cdot \mathbf{V}_i \rangle + \frac{\sqrt{g} B^{\zeta} B^{\theta}}{c} J_{\text{external}} \cdot \nabla \psi. \quad (27)$$

Similarly, Eq. (2) can be written as

$$[m_i N_i \langle B^2 \rangle] \frac{\partial \lambda}{\partial t} = -\langle \mathbf{B} \cdot \nabla \cdot \bar{\pi} \rangle - m_i N_i \nu_{in} \langle \mathbf{B} \cdot \mathbf{V}_i \rangle. \quad (28)$$

A qualitative assessment of the stability properties of the steady-state solutions (or fixed points) of the momentum balance equations can be provided by plotting the phase portrait³¹ consisting of the vector field of points that correspond to $\frac{\partial \Phi'}{\partial t}$ and $\frac{\partial \lambda}{\partial t}$ at each point, Φ' and λ on a two-dimensional grid and then converted to the E_r , $V_{||}$ plane. This is shown in Fig. 12. The red, blue, and green points correspond to the steady-state solutions shown in Fig. 11. The arrows surrounding the red and green points point to the steady-state solution, indicating stability. However, for the second solution in blue, the vectors point

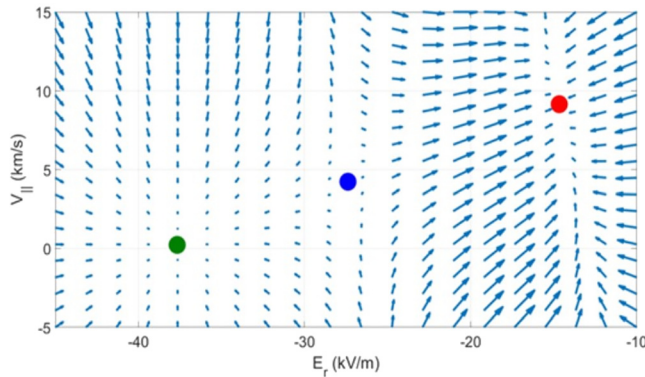


FIG. 12. A vector plot of the radial electric field and the parallel flow for a given radial current density. The magnitudes of the vectors correspond to the time derivatives. Locations for the steady-state solutions 1, 2, and 3 are marked with red, blue, and green dots, respectively.

toward the solution vertically but away from the solution horizontally. This implies that the second solution is unstable.

A quantitative analysis of the stability of fixed points of the momentum balance equations is provided by calculating the eigenvalues and eigenvectors of the nonlinear system.³¹ Stability is assessed by considering whether a small perturbation from the equilibrium point grows or decays in time. Considering perturbations around the equilibrium points λ^* and Φ^* ,

$$\lambda(t) = \lambda^* + \Delta\lambda(t), \quad (29a)$$

$$\Phi(t) = \Phi^* + \Delta\Phi(t), \quad (29b)$$

and expanding in a Taylor series about the fixed point, then

$$\frac{d}{dt} \begin{bmatrix} \Delta\lambda \\ \Delta\Phi \end{bmatrix} = \begin{bmatrix} \frac{\partial J_p}{\partial \lambda} & \frac{\partial J_p}{\partial \Phi} \\ \frac{\partial J_{||}}{\partial \lambda} & \frac{\partial J_{||}}{\partial \Phi} \end{bmatrix}_{\lambda^*, \Phi^*} \begin{bmatrix} \Delta\lambda \\ \Delta\Phi \end{bmatrix}, \quad (30)$$

where the higher order terms in the series have been neglected. J_p and $J_{||}$ are the right-hand sides of the poloidal and the parallel momentum balance Eqs. (27) and (28) divided by the coefficients multiplying $\frac{\partial \Phi}{\partial t}$ and $\frac{\partial \lambda}{\partial t}$, respectively. The 2×2 matrix in Eq. (30) is the Jacobian \mathbf{J} evaluated at each of the fixed points, λ^* and Φ^* . The solution to the equation above is in the form $e^{\gamma t} \mathbf{v}$, where $\mathbf{J} \cdot \mathbf{v} = \gamma \mathbf{v}$, γ is the eigenvalue and \mathbf{v} is the eigenvector. The eigenvalues are solved by calculating the determinant, $\det(\mathbf{J} - \gamma \mathbf{I}) = 0$, where \mathbf{I} is the identity matrix. A positive eigenvalue is an exponential growth away from the fixed point, indicating instability, while a negative eigenvalue is a decay back to the fixed point, indicating stability. Given the eigenvalues, the eigenfunctions \mathbf{v} can then be constructed.

The calculated eigenvalues for the three solutions shown in Fig. 12 are given in Table I. All the eigenvalues are real, and the eigenvalues for solutions 1 and 3 are both negative, demonstrating that they are both stable solutions to the momentum balance equations. However, solution 2 has one negative eigenvalue and one positive eigenvalue, which makes that fixed point an unstable saddle point.

TABLE I. Calculated eigenvalues for the three solutions that are the fixed points of the momentum balance equations.

Solution	1	2	3
γ_1	−4890	−4890	−4890
γ_2	−30 200	+10 000	−4390

Figure 13 shows the eigenvectors for the three fixed points shown in Fig. 12. Eigenvectors that correspond to stable eigenvalues are shown by green dashed lines; eigenvectors that correspond to an unstable eigenvalue are represented by a red dashed line. The steady-state solutions to the momentum balance equations are the red, blue, and dark green points for the top, middle, and bottom figures, respectively. The eigenvector arrows that point toward the fixed points show stability, and the arrows for the one unstable eigenvector point away from the fixed point. The black solid lines are the solutions to the time-dependent equations given in (27) and (28) with initial conditions that correspond to points on the boundary. The arrows show the direction of the solution toward or away from the fixed points.

As with other figures, the eigenvectors and time-dependent equations are first solved in Φ' and λ space and then converted to E_r and $V_{||}$. For the first fixed point, shown on the top of Fig. 13, all of the trajectories fall back to the stable equilibrium point shown in red. Note that from Table I, solution 1 has two eigenvalues with $|\gamma_2| > |\gamma_1|$. The larger amplitude eigenvalue γ_2 corresponds to the eigenvector with a positive slope, while the smaller eigenvalue corresponds to the eigenvector with a negative slope. Since the general solution is of the form $e^{\gamma t} \mathbf{v}$, for positive time $t > 0$, the larger negative eigenvalue dies off quickly and the trajectories approach the fixed point parallel to the eigenvector with the smaller eigenvalue. Similarly for time $t < 0$, the trajectories move away from the fixed point parallel to the eigenvector with the larger eigenvalue.

The eigenvectors and trajectories for solution 2, which is an unstable saddle point, are shown in the middle of Fig. 13. The eigenvector corresponding to the positive eigenvalue is shown in red. For this case, all the trajectories diverge away from the fixed point parallel to the unstable eigenvector for time $t > 0$. Similarly, for time $t < 0$, the trajectories become parallel to the stable eigenvector. Note that the eigenvectors agree with the vector plot of Fig. 12: the trajectory is toward the fixed point roughly parallel to the $V_{||}$ axis and away from the fixed point roughly parallel to the E_r axis. The last fixed point, solution 3, has two eigenvalues of roughly the same magnitude. This is the case where the viscous damping is negligible and only damping due to neutrals exists. When two eigenvalues are equal, then any vector on the plane can be composed of the sum of the two eigenvectors and in turn can be shown to be an eigenvector with that same eigenvalue.³¹ In that case, all trajectories are straight lines, and the fixed point is known as a star node. For solution 3, the eigenvalues are not exactly equal and close to the fixed point it can be seen that the trajectories bend toward the eigenvector with the smaller eigenvalue (the green dashed line with a positive slope).

By examining the Jacobian in Eq. (30), the physical mechanism behind the unstable equilibrium point for solution 2 can be understood. The unstable eigenvalue occurs when the term $\frac{\partial J_p}{\partial \Phi'}$ becomes positive, where J_p is the right-hand side of Eq. (27) divided by the coefficient multiplying $\frac{\partial \Phi}{\partial t}$. Alternatively, since $E_r \sim -\Phi'$, the unstable

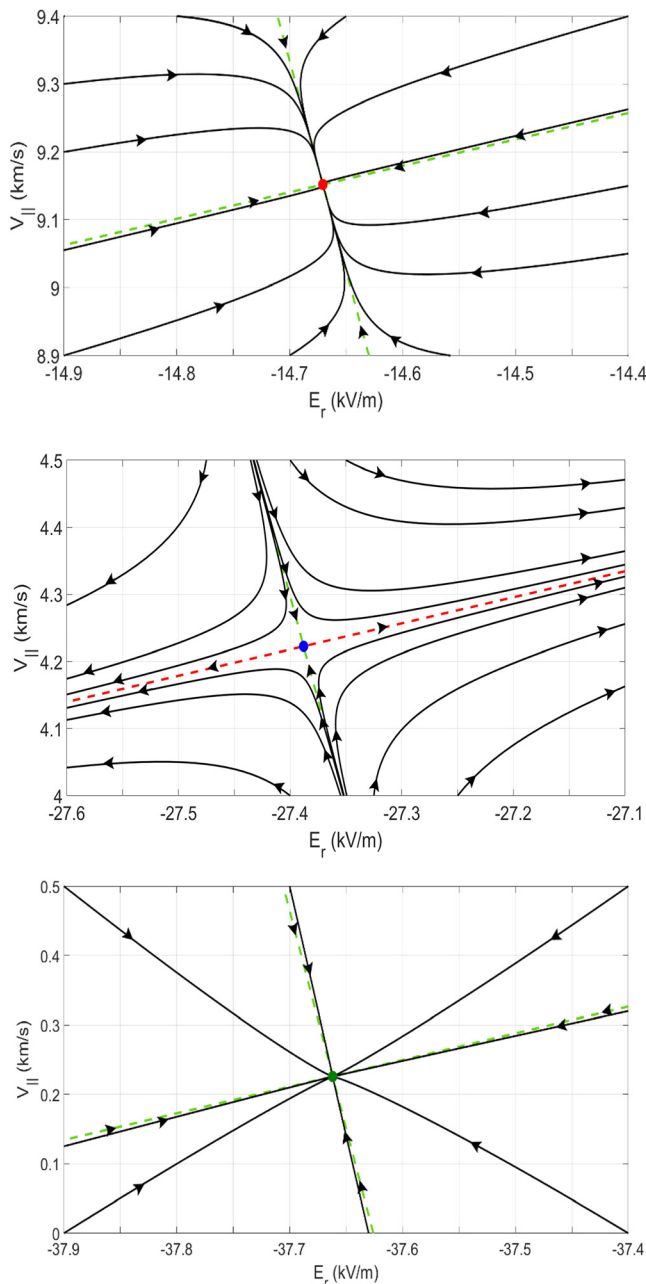


FIG. 13. Eigenvectors (dashed line) and trajectories (black solid line) of the time-dependent momentum balance equations near the three solutions (top corresponds to first or red solution, middle is the second or blue solution, and bottom is the third or dark green solution) shown in Fig. 11. Eigenvectors in green correspond to negative eigenvalues and denote stability, while eigenvectors in red correspond to positive eigenvalues and denote instability.

eigenvalue occurs when the derivative of J_p with the respect to the radial electric field is negative. Figure 14 shows a plot of J_p vs E_r for a fixed value of λ that corresponds to the second solution shown by the blue point. The first and the third solutions, shown by the green and

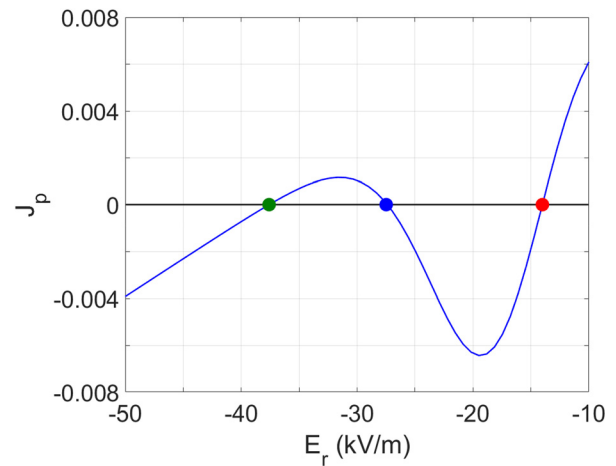


FIG. 14. J_p vs the radial electric field E_r for a fixed value of λ that corresponds to the blue unstable equilibrium point. J_p is the right-hand side of Eq. (26), the poloidal momentum balance equation, divided by the coefficient multiplying $\frac{\partial \psi}{\partial r}$. The locations of the two stable green and red points are approximate because they have different λ values.

red points, respectively, are in approximate locations because they have different λ values as seen in Figs. 11 and 12.

The two stable red and green points are in regions where $\frac{dJ_p}{dE_r} > 0$. From Eq. (27), J_p is proportional to the drive term $J_{\text{external}} \cdot \nabla \psi$, which in this case is a constant, minus the two damping terms due to viscosity and ion-neutral friction. A small perturbation of either of the two stable points to the right, to less negative E_r , lowers the damping and increases the value of J_p . That in turn increases the net drive on the system and pushes the electric field to a larger negative value back to the fixed point. Alternatively, a small perturbation to the left, to higher negative E_r , increases the damping and lowers the net drive. That pushes the electric field to a lower negative value back to the fixed point. For the unstable point in blue, the opposite happens. A perturbation to the right, to decreasing negative E_r , increases the damping (see Fig. 6, for example, to the left of the maximum in viscosity for negative electric fields) and forces J_p to decrease. That lowers the net drive so that E_r is forced to an even smaller negative value. The system won't find another equilibrium until it converges onto the red point. Similarly, a perturbation to the left, to increasing negative E_r , lowers the damping and forces J_p to increase. This in turn increases the net drive forcing the electric field to even larger negative values. In this case, the system won't find another equilibrium point until it converges onto the green point. From this discussion, it can be concluded that the condition for instability $\frac{dJ_p}{dE_r} < 0$ occurs when the derivative of the total poloidal damping with respect to the electric field is positive.

The previous analysis was done with a fixed value of the current density. To examine how Eqs. (27) and (28) transition between solutions, it is worthwhile to consider the case when the external current density is time dependent. The waveform is a simple triangle wave so that the radial current density $J_{\text{external}} \cdot \nabla \psi$ linearly increases with time to a maximum of 1.4×10^{11} and then linearly decreases back to zero. The maximum current density is chosen specifically so that the only solution is in solution 3.

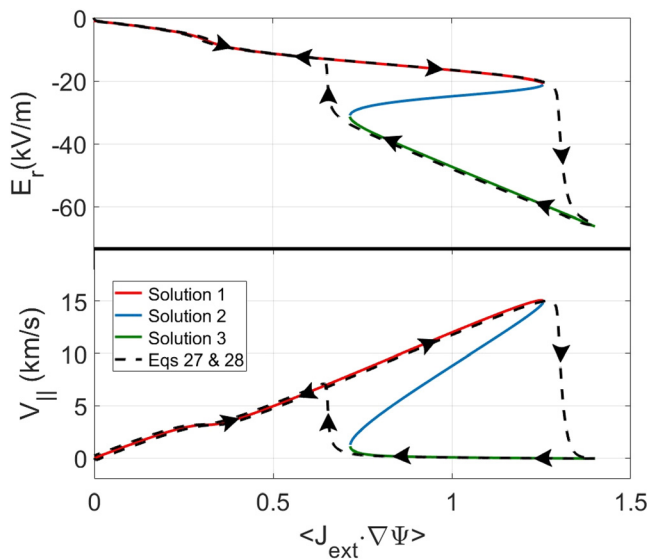


FIG. 15. Evolution of E_r and $V_{||}$ as a function of the external radial current density (divided by 10^{11}) as $J_{\text{external}} \cdot \nabla \Psi$ increases linearly up to a value of 1.4×10^{11} and then ramps back down to zero.

The evolution in time of E_r and $V_{||}$ is shown in Fig. 15. Also in the figure are the same steady-state solutions that are shown in Fig. 11. As the radial current density increases, both quantities increase and follow the same curves as solution 1 so that the solutions are always stable. Once the radial current density increases past the point where solution 1 ends, there is a jump to solution 3. During this fast transition, there is a jump in the radial electric field from -20 kV/m to greater than -60 kV/m, similar to what may be observed during an L–H transition. During this fast transition, the radial current density is roughly constant, and the parallel flow abruptly drops from 15 km/s to zero. After the radial current density reaches the maximum value of 1.4×10^{11} , the peak of the triangle waveform, it decreases while the evolution of E_r and $V_{||}$ continues on solution 3. Below a value of 0.72×10^{11} , the radial electric field and the parallel flow take another jump back to solution 1. Again, during this fast transition, the radial current density is roughly constant while E_r drops from -30 to -13 kV/m and $V_{||}$ jumps from near zero up to 7 km/s. As the radial current density continues to decrease, both continue along solution 1 back to the initial values. Throughout the ramp-up and ramp-down of the radial current density, the solutions never evolve on the path of solution 2, which is unstable. Note that for the hysteresis shown in the plasma flow, the radial current density for the transition from solution 1 to solution 3 is at a higher value than for the back transition from solution 3 to solution 1.

VII. SUMMARY AND DISCUSSION

In this paper, we highlight the role of the parallel flow in determining the resonant electric field in HSX as well as the influence of $V_{||}$ on the equilibrium and stability of the momentum balance equations. The essential role of the parallel flow is a result of the quasi-helical symmetry of the magnetic field, which has minimal parallel viscous damping in the direction of quasisymmetry. The time-dependent momentum balance equations in Hamada coordinates with linear

viscosity and neutral damping allow for an analytic solution that separates the flow into slow and fast damping times. The evolution of the parallel flow is strongly dominated by the slow damping rate characteristic of the damping in the direction of quasisymmetry. The radial electric field evolution is dominated by the fast damping time at the plasma core and an increasing contribution of the slow damping rate toward the plasma edge. For the QHS configuration, the contribution of viscosity to the slow rate is so small that neutral damping dominates across the plasma radius. For the Mirror and F14 configurations, neutral damping does not have quite as much influence on the slow rate as in the QHS configuration. Neutral damping has little impact on the fast damping time for all configurations.

Based on Shaing's model of nonlinear viscosity, an analytic expression is obtained that relates the parallel flow to the ion resonant electric field E_{res} . This expression indicates that parallel flows on the order of or greater than the ion thermal velocity can have a significant impact on E_{res} . While multiple tokamaks and stellarators have demonstrated experimentally that E_{res} is determined by the leading terms in the Fourier spectrum of the magnetic field, to date, there has been no experimental data that shows how E_{res} depends on the parallel flow. From the steady-state momentum balance equations, E_{res} for the QHS configuration is shown to be over a factor of 2 greater than the value when $V_{||} = 0$. Increasing the viscous damping in the direction of the quasisymmetry (and thereby degrading that symmetry), such as occurs in the Mirror configuration, lowers the parallel flow and in turn lowers the ion resonant electric field. Similarly, increasing the neutral damping also reduces $V_{||}$ and E_{res} . A plot of E_{res} as a function of $V_{||}$ for three magnetic configurations in HSX and different levels of neutral damping shows good agreement with the analytic expression. The results suggest the possibility of measuring different resonant electric fields for different configurations in HSX, even though they share the same large $(n, m) = (4, 1)$ mode in the magnetic field spectrum, because the additional $m = 0$ terms in the spectrum for the Mirror and F14 configurations do not alter the poloidal viscosity.

The only damping mechanisms considered in this paper are parallel viscosity and ion-neutral damping. When the damping is small, the parallel flow can be much larger than the ion thermal velocity. At large flow speeds, the convective term $V \cdot \nabla V$ in the momentum balance equations may need to be considered; it has not been included in this work. The possibility of shock fronts occurring in the plasma has also not been considered. Alternatively, there may be damping mechanisms other than the two considered here, such as turbulent Reynolds stress^{32,33} or perpendicular viscosity^{34,35} that may limit the flow in the QHS configuration of HSX. Indeed, experiments at $B = 0.5$ T indicated that the measured slow decay rate and the radial conductivity were roughly an order of magnitude higher than the model calculations.⁵ Artificially increasing the neutral density by an order of magnitude brought the measurements and modeling into better agreement. This result suggests that there may be sources of anomalous flow damping in HSX.

The stability of three steady-state solutions to the momentum balance equations at a fixed radial current density is analyzed for the QHS configuration with ten times the experimental neutral density. This increased neutral density serves as an “*ad hoc*” model for the enhanced flow damping that may exist in HSX. A phase portrait is generated by plotting on a two-dimensional E_r , $V_{||}$ grid the time

derivatives of those quantities as a vector field. The portrait indicates that the first and the third solutions are stable, but that the second solution appears to be unstable. A quantitative analysis is performed based on the Jacobian of the time-dependent equations. Two negative eigenvalues are found for the first and the third of the three solutions, indicating that they are in fact stable. The second solution has one negative and one positive eigenvalue, indicating that it is an unstable saddle point. The eigenvectors of the Jacobian yield insight into how the time-dependent equations move toward or away from the fixed point. Finally, examining the components of the Jacobian gives insight into the physical mechanism of how an equilibrium solution can be unstable. An unstable solution exists when the derivative of the total poloidal damping with respect to the radial electric field is positive.

A hysteresis in both E_r and $V_{||}$ occurs when the radial current density is linearly increased to a maximum and then decreased back to zero. Jumps in the radial electric field and parallel flow are observed as the radial current density drives the evolution from one stable point to the next. The transition from solution 1 to solution 3 is at a higher value for the radial current density than for the back transition from solution 3 to solution 1. This is similar to the data obtained on the TU-Heliac shown in Fig. 7(a) of Ref. 19.

Finally, it should be noted that neoclassical codes such as PENTA do not consider the effect of the parallel flow on the ion resonant electric field. An example can be seen in Fig. 3.12 in Ref. 36, where $V_{||}$ is calculated as a function of E_r for similar parameters in HSX as assumed here. Parallel flows as high as 150 km/s can be seen in that figure, much higher than the ion thermal velocity. Yet, the location of the ion resonant electric field is based solely on the magnetic field spectrum. Using the ambipolarity constraint to solve for E_r , the parallel flow as a function of r/a is shown in Ref. 11, where $V_{||}$ above the ion thermal velocity can be seen for ion root plasmas. Experimental evidence that the ion resonant electric field is dependent on the parallel flow might lead to a reconsideration of how the parallel flows and ambipolar electric fields are calculated in codes such as PENTA.

ACKNOWLEDGMENTS

The authors would like to acknowledge useful discussions with C. C. Hegna, S. T. A. Kumar, D. T. Anderson, K. Likin, B. J. Faber, C. Lu, A. L. F. Thornton, and A. Wolfmeister. This work was supported by the U.S. Department of Energy under Grant No. DE-FG02-93ER54222.

AUTHOR DECLARATIONS

Conflict of Interest

The authors have no conflicts to disclose.

Author Contributions

Dimitri N. Michaelides: Formal analysis (equal); Investigation (lead); Methodology (equal); Supervision (supporting); Visualization (lead); Writing – original draft (lead); Writing – review & editing (supporting). **Joseph N. Talmadge:** Conceptualization (lead); Formal analysis (equal); Investigation (supporting); Methodology (equal); Supervision (lead); Visualization (supporting); Writing – original draft (supporting); Writing – review & editing (lead).

DATA AVAILABILITY

The data that support the findings of this study are available from the corresponding author upon reasonable request.

REFERENCES

- M. Landreman, S. Buller, and M. Drevlak, *Phys. Plasmas* **29**, 082501 (2022).
- A. Bader, D. T. Anderson, M. Drevlak, B. J. Faber, C. C. Hegna, S. Henneberg, M. Landreman, J. C. Schmitt, Y. Suzuki, and A. Ware, *Nucl. Fusion* **61**, 116060 (2021).
- K. H. Burrell, E. J. Doyle, P. Gohil, R. J. Groebner, J. Kim, R. J. La Haye, L. L. Lao, R. A. Moyer, T. H. Osborne, W. A. Peebles, C. L. Rettig, T. H. Rhodes, and D. M. Thomas, *Phys. Plasmas* **1**, 1536 (1994).
- S. Ding, A. M. Garofalo, M. Knolker, A. Marinoni, J. McClenaghan, and B. A. Grierson, *Nucl. Fusion* **60**, 034001 (2020).
- S. P. Gerhardt, J. N. Talmadge, J. M. Canik, and D. T. Anderson, *Phys. Plasmas* **12**, 056116 (2005).
- M. Coronado and J. N. Talmadge, *Phys. Fluids B* **5**, 1200 (1993).
- A. Briesemeister, K. Zhai, D. T. Anderson, F. S. B. Anderson, J. Lore, and J. N. Talmadge, *Contrib. Plasma Phys.* **50**, 741 (2010).
- S. T. A. Kumar, J. N. Talmadge, T. J. Dobbins, F. S. B. Anderson, K. M. Likin, and D. T. Anderson, *Nucl. Fusion* **57**, 036030 (2017).
- T. J. Dobbins, S. T. A. Kumar, J. N. Talmadge, and D. T. Anderson, *Nucl. Fusion* **59**, 046007 (2019).
- D. A. Spong, *Phys. Plasmas* **12**, 056114 (2005).
- J. Lore, W. Guttenfelder, A. Briesemeister, D. T. Anderson, F. S. B. Anderson, C. B. Deng, K. M. Likin, D. A. Spong, J. N. Talmadge, and K. Zhai, *Phys. Plasmas* **17**, 056101 (2010).
- K. C. Shaing and E. C. Crume, Jr., *Phys. Rev. Lett.* **63**, 2369 (1989).
- K. C. Shaing, *Phys. Fluids B* **5**, 3841 (1993).
- R. R. Weynants, S. Jachmich, and M. Van Schoor, *Fusion Sci. Technol.* **47**, 202 (2005).
- R. J. Taylor, M. L. Brown, B. D. Fried, H. Grote, J. R. Liberati, G. J. Morales, P. Pribyl, D. Darrow, and M. Ono, *Phys. Rev. Lett.* **63**, 2365 (1989).
- H. Dahi, J. N. Talmadge, and J. L. Shohet, *Phys. Rev. Lett.* **80**, 3976 (1998).
- J. N. Talmadge and S. P. Gerhardt, *Phys. Plasmas* **12**, 072513 (2005).
- M. Coronado and J. G. Trejo, *Phys. Fluids B* **2**, 530 (1990).
- H. Takahashi, M. Yokoyama, S. Kitajima, Y. Tanaka, H. Utoh, and M. Sasao, *Plasma Phys. Controlled Fusion* **48**, 39 (2006).
- S. Kitajima *et al.*, *Nucl. Fusion* **53**, 073014 (2013).
- S. Hamada, *Nucl. Fusion* **2**, 23 (1962).
- J. N. Talmadge, V. Sakaguchi, F. S. B. Anderson, D. T. Anderson, and A. F. Almogri, *Phys. Plasmas* **8**, 5165 (2001).
- J. M. Canik, D. T. Anderson, F. S. B. Anderson, C. Clark, K. M. Likin, J. N. Talmadge, and K. Zhai, *Phys. Plasmas* **14**, 056107 (2007).
- S. T. A. Kumar, T. J. Dobbins, J. N. Talmadge, R. S. Wilcox, and D. T. Anderson, *Plasma Phys. Controlled Fusion* **60**, 054012 (2018).
- D. Heifetz, D. Post, M. Petravic, J. Weisheit, and G. Bateman, *J. Comput. Phys.* **46**, 309 (1982).
- J. L. Velasco, J. A. Alonso, I. Calvo, and J. Arévalo, *Phys. Rev. Lett.* **109**, 135003 (2012).
- K. C. Shaing, S. P. Hirshman, and J. D. Callen, *Phys. Fluids* **29**, 521 (1986).
- M. Coronado and H. Wobig, *Phys. Fluids* **29**, 527 (1986).
- A. Briesemeister, K. Zhai, D. T. Anderson, F. S. B. Anderson, and J. N. Talmadge, *Plasma Phys. Controlled Fusion* **55**, 014002 (2013).
- K. C. Shaing and J. D. Callen, *Phys. Fluids* **26**, 3315 (1983).
- S. H. Strogatz, *Nonlinear Dynamics and Chaos* (Perseus Books, Massachusetts, 1994).
- P. Helander and A. N. Simakov, *Phys. Rev. Lett.* **101**, 145003 (2008).
- R. S. Wilcox, J. N. Talmadge, D. T. Anderson, F. S. B. Anderson, and J. D. Lore, *Nucl. Fusion* **56**, 036002 (2016).
- D. E. Hastings, W. A. Houlberg, and K. C. Shaing, *Nucl. Fusion* **25**, 445 (1985).
- H. Maassberg, R. Burhenn, U. Gasparino, G. Kühner, H. Ringler, and K. S. Dyabilin, *Phys. Fluids B* **5**, 3627 (1993).
- J. Lore, Ph.D. thesis (University of Wisconsin-Madison, 2010).